

# Impact of Fault Impedance and Duration on Transient Response of Hybrid AC/DC Microgrid

*Younes Seyedi\**, *Jean Mahseredjian*, and *Houshang Karimi*

*Department of Electrical Engineering, Polytechnique Montreal, Montreal QC H3T 1J4, Canada.*

---

## ARTICLE INFO

### Keywords:

Distributed energy resources  
 Fault  
 Hybrid AC-DC Microgrid  
 Protection  
 Transient  
 Voltage stability

## ABSTRACT

This paper proposes a mechanism for time-frequency analysis of post-fault transient response in hybrid AC/DC microgrids. The proposed mechanism is based on the continuous wavelet transform of the electromagnetic transient (EMT) simulation data in grid-connected and islanded modes of operation. The proposed mechanism is used to evaluate the impact of fault parameters on the post-fault voltage recovery and to estimate the critical clearance time of the faults. Moreover, a simulation benchmark is developed that involves different types of distributed energy resources (DERs) including solar photovoltaic (PV), wind, and battery energy storage systems. The developed microgrid benchmark is implemented in EMTP software and extensive simulation results are analyzed to obtain insights into the voltage recovery and transient response of hybrid AC/DC microgrid subject to faults.

---



---

## 1. Introduction

Microgrids are among the key components of the smart grid technology that can provide consumers with clean and sustainable energy even in the absence of the main grid. As more renewables, distributed energy resources (DERs), and electric vehicles (EVs) are deployed in low-voltage distribution networks, new methods and structures are developed to leverage reliable and economic operation of microgrids [1]. In particular, microgrids are evolving into hybrid AC/DC microgrids to accommodate higher penetration of renewables and to supply power to AC and DC loads with a fewer number of converters [2]. Hybrid AC/DC microgrids can reduce the conversion losses and harmonics as compared with their AC counterparts [2], [3].

A typical hybrid microgrid consists of AC subgrids, DC subgrids, and interlinking converters (ICs) that connect the AC subgrids to the DC subgrids [4]. The ICs are capable of bidirectional power exchange between the subgrids to ensure voltage stability in the DC subgrid or frequency stability in the AC subgrid [5]. In contrast with traditional distribution systems, hybrid microgrids are deemed to be complex systems in terms of energy management, control and protection strategies [6], [7].

The hybrid microgrids can be subject to different types of temporary faults which may occur in either of the subgrids while they operate in grid-connected or islanded mode. Moreover, the subgrids may employ different types of DERs with different control strategies (e.g., PQ, PV) that affect their disturbance-ride-through capability [8]. It is shown that a high penetration of

---

\* Corresponding author

E-mail addresses: younes.seyedi@polymtl.ca (Y. Seyedi), jean.mahseredjian@polymtl.ca (J. Mahseredjian), houshang.karimi@polymtl.ca (H. Karimi)

renewables in the subgrids affects the protection reliability and complicates the fault management [9]. Efforts have been made to address some protection issues in hybrid microgrids [8, 10, 11].

The study presented in [8] shows that hybrid microgrids with induction motors tend to exhibit post-disturbance oscillations in the islanded mode of operation. A controller for energy storage systems is developed in [8] to damp low-frequency oscillations due to severe disturbances. A simplified protection scheme is proposed in [10] to detect and isolate the faulty side of the IC. It employs discrete Fourier transform (DFT) of the oscillating current measured at the DC side of the IC to detect faults at the AC side. However, this scheme may fail in hybrid microgrids that do not exhibit oscillations in the DC side voltage/current during the fault. The study in [11] analyzes the impact of asymmetric faults on the DC side voltage, and proposes a control strategy for the IC to compensate for the negative and zero sequence components and attenuate the DC side power fluctuations.

Despite the recent advances, a comprehensive analysis of post-fault transients and voltage stability is required for resilient operation of hybrid microgrids. In particular, the previous fault studies in the literature lack a qualified mechanism for analysis of fault-induced transients when either of the AC or DC subgrids operates in the islanded mode. In this regard, time-frequency analysis methods can be helpful, for instance, the wavelet transform has shown promising results for different protection applications in AC microgrids including: detection and feature extraction of disturbances [12], fault classification [13], fault detection and localization [14-17].

This paper presents a mechanism for analysis of the post-fault transient response of hybrid AC/DC microgrids. The proposed mechanism consists of time-domain electromagnetic transient (EMT) simulations and the continuous wavelet transform. This mechanism is used to assess the impact of fault resistance, location and duration on the post-fault voltage stability. The proposed mechanism facilitates numerical estimation of the critical clearance time (CCT) when either of the AC/DC subgrids operates in the islanded mode.

The main contributions of this paper are as follows: 1) It is shown that the interactions between the DERs and the IC may lead to major post-fault disturbances or oscillations in the islanded subgrid. As a consequence, if

the fault clearance time exceeds a critical value, then the voltage of the islanded subgrids cannot be stabilized. 2) Since many local controllers are involved in the post-fault transient response of the hybrid microgrids, theoretical assessment of the CCT is not a mathematically tractable problem. To overcome this important challenge, a mechanism is developed which numerically estimates the CCT based on the continuous wavelet transform of the EMT simulation data. In the proposed mechanism, the CCT estimation is independent of the microgrid topological conditions. Hence, it can be applied to large-scale hybrid microgrids with arbitrary number of DERs and multiple ICs.

---

## 2. Post-Fault Transient Response of Hybrid AC/DC Microgrids

The post-fault transient response of hybrid microgrids can have a significant impact on the operation of the protective devices such as relays, and also affects the voltage stability in the islanded AC/DC subgrid. Therefore, it is necessary to analyze the transients that emanate from temporary faults in order to ensure the stability and resiliency of the microgrid. In general, the transient response of hybrid microgrids to temporary faults depends on:

- 1) Location, duration and resistance of the fault
- 2) Operation mode of the subgrids
- 3) Type and operating conditions of DERs
- 4) Control parameters of DERs and the IC

The simulation results presented in Section 4 reveal that the location and resistance of the fault within a subgrid may significantly affect the extent and volatility of the voltage transients. Moreover, a low resistance fault which creates major post-fault voltage disturbances may also lead to voltage transients in the healthy subgrid. For a given fault location, time-domain EMT simulations can be carried out to assess the impact of fault duration and resistance on the post-fault disturbances.

The operation mode of the subgrids plays a crucial role in their post-fault behavior as the islanded subgrids have lower inertia which is translated to a higher degree of sensitivity to disturbances. In the islanded mode, the voltage stability not only depends on the grid-forming DG systems but also on the power transfer capability of the IC. The DC subgrid may employ battery devices for the load sharing and voltage control [18] while the AC subgrid may use droop-controlled DG systems that uti-

lize reliable DC sources such as energy storage system (ESS) [19].

The type and control parameters of the DERs and the IC have remarkable impacts on the voltage and current transients that emerge after the fault clearance, particularly when a subgrid operates in the islanded mode. For example, wind and solar PV systems can be controlled based on the maximum power point tracking (MPPT) method which leads to variable real power injection and limited reactive power. Moreover, the droop gain of the IC affects the maximum real power that can be exchanged between the subgrids [20, 21], which in turn limits the contribution of the IC in the voltage/frequency recovery.

It is known that the fault duration has an impact on the post-fault behavior of AC microgrids that operate in the islanded mode [22]. In the case of hybrid microgrids, analysis of the impact of the fault resistance and duration is a more complicated task [7]. For example, the fault-induced disturbances in the grid-connected subgrid can also disturb the islanded subgrid (which has a lower inertia) via the IC. Therefore, the protective devices in the islanded subgrid may trigger a false trip. It is thus necessary to identify the source of faults in a timely manner before false trips take place in the healthy subgrid. Once the faulty node is identified, preventive actions such as disconnection of the IC can be launched by the backup protection system.

### 3. Estimation of the Critical Clearance Time

The analysis of the fault-induced transients and the subsequent post-fault voltage stability require detailed modeling of different components of the hybrid microgrid. It should be highlighted that this analysis is not a mathematically tractable problem due to complex interactions between different DERs, the ICs and the loads. Elaborate simulation-based methods are required to overcome this challenge. In this paper, it is shown that EMT simulations are effective tools that provide the necessary data for time-frequency analysis of fault-induced transients. Moreover, they pave the way for numerical assessment of the post-fault voltage recovery in hybrid AC/DC microgrids. Estimation of the CCT, sensitivity assessment based on the fault location and resistance are among important applications of the simulation-based methods.

The CCT is an important parameter that should be taken into account in the design of protection schemes.

The CCT is related to the post-fault transient response of the hybrid microgrids and is defined as the maximum duration of fault that leads to sufficiently small post-fault voltage transients in both AC and DC subgrids. The CCT can be analyzed for a given fault resistance and fault location, i.e., the CCT may change if the fault location or resistance change.

The transients that exist in the post-fault voltage/current measurements are inherently non-stationary signals. In fact, the post-fault voltage/current signals consist of different components with variable magnitude, frequency, and duration. The continuous wavelet transform is an effective tool for high-fidelity analysis of such transient signals. The wavelet transform is helpful in tracing transients and oscillations that may exist in the post-fault voltage and current signals. An advantage of the wavelet transform over the windowed Fourier transform is that it can accurately localize the short-duration and high-frequency signal components such as fault-induced voltage transients [23].

Suppose the fault occurs at the time instant  $t = t_f$  and is cleared after  $T_f$  s. In EMT simulations, the fault instant should be large enough to allow the DERs and the IC operate under their steady-state conditions. The continuous wavelet transforms of the post-fault voltages are obtained as:

$$\vartheta_{dc}(s, \tau) = \frac{1}{s} \int_{t_f+T_f}^{+\infty} \Psi^* \left( \frac{t-\tau}{s} \right) V_{dc}(t) dt \quad (1)$$

$$\vartheta_{ac}(s, \tau) = \frac{1}{s} \int_{t_f+T_f}^{+\infty} \Psi^* \left( \frac{t-\tau}{s} \right) v_{ac}(t) dt \quad (2)$$

where  $\Psi(t)$  denotes the wavelet and the superscript  $(.)^*$  represents the complex conjugate.  $V_{dc}(t)$  and  $v_{ac}(t)$  in (1) and (2) denote the instantaneous voltage signals of the DC and AC subgrids, respectively.

The AC dispersion for the AC subgrid is defined as follows

$$\delta_{ac}(\tau) = \left| 1 - \frac{1}{(w_u - w_l)} \int_{s_0-w_l}^{s_0+w_u} \frac{|\vartheta_{ac}(s, \tau)|^2}{V_{ac,n}^2} ds \right| \quad (3)$$

where  $w_l$  and  $w_u$  denote the lower and upper limits around the fundamental scale  $s_0$ , and  $V_{ac,n}$  denotes the

nominal voltage of the AC subgrid. The fundamental scale satisfies the following relationship

$$s_0 = \frac{F_c}{f_0} \quad (4)$$

where  $F_c$  is the center frequency and depends on the associate wavelet  $\Psi$ .  $f_0$  in (4) denotes the nominal frequency of the AC subgrid, e.g., 60 Hz. The limits  $w_u$  and  $w_l$  should correspond to a narrow range around the fundamental frequency  $f_0$ . Since the sampling rate of the EMT simulation results are known, the scale-to-frequency conversion method can be employed to determine which scales are around  $f_0$ . Therefore, the limits can be estimated as:

$$w_l = \min\{s | s > s_0\}$$

$$w_u = \max\{s | s < s_0\}$$

According to (3), the AC dispersion estimates the time-series of the total energy of the transient components excluding the fundamental component at  $f_0$ . Therefore, when the voltage of the AC subgrid becomes stable the transient components vanish and the AC dispersion is asymptotic to zero.

The DC dispersion for the DC subgrid is defined as the following time-series:

$$\delta_{dc}(\tau) = \frac{1}{s_{max} - s_{min}} \int_{s_{min}}^{s_{max}} |\vartheta_{dc}(s, \tau)|^2 ds \quad (5)$$

Where  $s_{min}$  and  $s_{max}$  respectively denote the minimum and maximum scales and can be calculated using algorithms that account for the energy spread of the wavelet over the time and frequency [24]. Based on (4), the DC dispersion calculates the time-series of the total energy of the transient components given that the DC component is filtered by the wavelet transform in (1). The DC dispersion approaches zero when the post-fault DC voltage has no oscillatory component.

An advantage of the AC/DC dispersion parameters is that they can be used to decompose and quantify the transient components of the post-fault voltage data. In this setting, the CCT can be defined as:

$$\text{CCT} := \max\{T_f \mid \delta_{ac/dc}(\tau) < \Delta_{ac/dc}, \forall \tau > \alpha + t_f + T_f\} \quad (6)$$

where the parameter  $\alpha$  is the decay time and should satisfy:

$$\alpha \gg T_f$$

The parameters  $\Delta_{ac}$  and  $\Delta_{dc}$  in (6) respectively denote the AC and DC dispersion thresholds.

The definition given in (6) is justified based on following observations: when the AC and DC voltages are within their acceptable range the dispersion parameters approach zero. When either of the AC or DC voltages becomes oscillatory or does not return to the acceptable range, the corresponding dispersion parameter recedes from zero. Therefore, the post-fault voltage recovery implies a small dispersion and vice versa. Moreover, the dispersion parameters possess superior localization in time domain (as the continuous wavelet transform does), hence, they can accurately extract the interval of the post-fault voltage disturbances.

The dispersion thresholds can be numerically evaluated to obtain accurate estimates of the CCT. To this aim, a detailed EMT simulation is carried out where the AC and DC subgrids initially operate under the nominal conditions. When the network operates in the steady-state, a load change occurs which yields the maximum acceptable power mismatch. The AC and DC dispersion parameters are then calculated for the post-event interval. The calculated parameters represent the boundaries of the tolerable voltage deviations. Hence, the dispersion thresholds should satisfy the following:

$$\Delta_{ac/dc} > \delta_{ac/dc}(\tau | \tau \gg \tau_e)$$

where  $\tau_e$  shows the instant of the maximum power mismatch.

The CCT for a given fault location can be estimated using Algorithm 1. In this algorithm,  $R_f$  denotes the fault resistance,  $T_m$  shows the maximum duration, and  $\beta$  is the search tolerance. The algorithm starts with the maximum fault duration and evaluates the dispersion parameters after each round of simulation. If both of the AC and DC dispersion parameters are less than their thresholds, then the fault clearance does not lead to persistent disturbances and the lower boundary of the search interval, denoted by  $T_s$ , is updated. Otherwise, the upper boundary of the search interval, denoted by  $T_i$ , is updated. A new EMT simulation is carried out with the fault duration equal to the average of the boundary times, as stated in step 11 of Algorithm 1. This process continues until the length of the search interval, i.e.,  $T_i - T_s$  becomes less than the search tolerance  $\beta$ . The accuracy of the CCT estimation is thus controlled by the value of  $\beta$ . A lower  $\beta$  implies more accurate estimates, however, it increases the estimation time. In practical AC microgrids, the maximum duration is normally greater than

or equal to 100 ms, thus  $\beta = 1$  ms yields reliable estimates of the CCT without imposing a high computational burden.

Based on Algorithm 1, the number of EMT simulations required for the estimation of the CCT is given by:

$$N_{sim} = \left\lceil \log_2^{T_m/\beta} + 1 \right\rceil \quad (7)$$

According to (7), the estimation time which is proportional to the number of EMT simulations is a function of the logarithm of the maximum duration. While a fixed value of  $T_m$  can be used regardless of the fault location, a more efficient strategy can exploit a dynamic  $T_m$  depending on the fault location.

---

**Algorithm 1: Estimation of the CCT for a given fault location**

---

**Inputs:**  $t_f, R_f, T_m, \Delta_{ac}, \Delta_{dc}, \alpha, \beta$

---

**Initialize:** Set  $T_f = T_m, T_s = 0, T_i = T_m$

---

- 1: Run EMT simulation with the fault instant  $t = t_f$  and the fault duration  $T_f$ . Save  $V_{dc}(t)$  and  $v_{ac}(t)$ .
  - 2: Calculate the dispersion parameters using (3) and (5).
  - 3: if  $\delta_{ac/dc}(\tau) < \Delta_{ac/dc}, \forall \tau > \alpha + t_f + T_f$ , then
  - 4:  $T_s \leftarrow T_f$
  - 5: else
  - 6:  $T_i \leftarrow T_f$
  - 7: End if
  - 8: If  $T_i - T_s \leq \beta$ , then
  - 9: CCT =  $T_f$  and terminate.
  - 10: else
  - 11:  $T_f \leftarrow (T_s + T_i)/2$  and go to 1.
  - 12: End if
- 

**Output:** CCT

---

The computational burden of EMT simulations depends on the size of the microgrid, the number of DERs and ICs, and the estimation parameters  $T_m$  and  $\beta$ . While it is not possible to completely eliminate the burden of the time-domain simulations, system designers can take advantage of Algorithm 1 to significantly reduce the burden of simulations. Moreover, the proposed mechanism can help the network operators to adapt the protection system schemes to the worst-case scenarios, e.g., when the lowest CCT is observed.

#### 4. Simulation Results

The performance of our proposed method is verified based on a hybrid microgrid benchmark with the diagram shown in Fig. 1. The DC and AC subgrids are connected to a medium voltage (MV) AC grid at the nominal voltage of 12.47 kVLL. Electromagnetic Transients Program (EMTP) is used for accurate simulations of the

transients in the test microgrid [25]. The simulation benchmark consists of detail models of DERs and their control components, including switching devices and inverters, dq-frame voltage and current control loops, phased-locked loops, etc. The simulation parameters for different components of the test microgrid are given in Table 1. The time-domain EMT simulation data are analyzed using the Morse wavelet with time-bandwidth product equal to 120 and symmetry parameter equal to 3 [26]. This setting narrows the wavelet filter in frequency and widens the central portion of the filter in time.

The DC subgrid has a nominal voltage of 600 V and consists of a solar PV system connected to node  $D_3$  and a battery at node  $D_5$ . The loads in the DC subgrid are identical and have a resistance equal to 360  $\Omega$ . The AC subgrid has a nominal voltage of 120 V and involves a DFIG wind turbine at node  $C_8$ , two DG systems at nodes  $C_7$  and  $C_{10}$ , and a solar PV system which is connected to node  $C_4$ . The DG systems in the AC subgrid use an ESS as the source of power. In the islanded AC subgrid the DG units play the role of grid-forming inverters by adopting a droop control method to maintain the voltage and frequency at their reference values [27], [28]. The loads and the line parameters of the AC subgrid comply with a commercial feeder proposed in the North American version of the CIGRE low-voltage distribution network benchmark [29]. The constant power loads are suggested in [29] for the low-voltage benchmark systems that incorporate renewable and distributed energy resources. Moreover, the proposed detection and estimation mechanism is independent of the load models. Hence, other types of microgrid loads, e.g., dynamic loads, can be simulated without affecting the performance of the proposed mechanism. Different scenarios have been simulated for analysis of the impact of the faults on the transient response of the test microgrid. The parameters of the simulation scenarios are summarized in Table 2. If applicable, the DC subgrid becomes islanded at  $t = 1$  s and the AC subgrid becomes isolated from the MV grid at  $t = 1.5$  s.

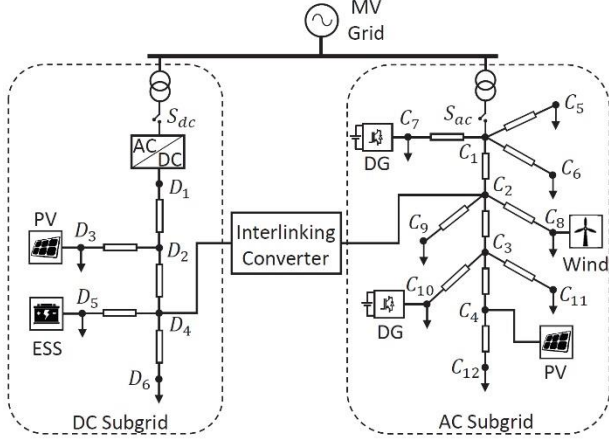


Fig. 1: The single-line diagram of the hybrid AC/DC microgrid benchmark

Table 1: THE CONTROL PARAMETERS OF THE TEST HYBRID AC/DC MICROGRID

System/Node	Parameter	Value
PV/ $D_3$	Capacity (kW)	3
	Irradiance ( $\text{W}/\text{m}^2$ )	500
ESS/ $D_5$	State of charge (%)	90
	Capacity (kWh)	10
DG/ $C_7$	Real power setpoint (kW)	10
	Reactive power setpoint (kVAr)	22
	Frequency droop gain ( $\text{Hz}/\text{W}$ )	$10^{-5}$
	Voltage droop gain ( $\text{V}/\text{VAr}$ )	$10^{-4}$
	Filter inductor (mH)	1
	Filter Capacitor ( $\mu\text{F}$ )	1
	Battery nominal voltage (V)	600
	Battery capacity (kWh)	50
Wind/ $C_8$	Capacity (kVA)	50
	Wind speed (m/s)	10
	Control mode	Q-control
	Reactive power setpoint (kVAr)	0
DG/ $C_{10}$	Real power setpoint (kW)	10
	Reactive power setpoint (kVAr)	22
	Frequency droop gain ( $\text{Hz}/\text{W}$ )	$10^{-5}$
	Voltage droop gain ( $\text{V}/\text{VAr}$ )	$10^{-4}$
	Filter inductor (mH)	1
	Capacitor ( $\mu\text{F}$ )	1
	Battery nominal voltage (V)	600
	Battery capacity (kWh)	50
PV/ $C_4$	Capacity (kVA)	30
	Irradiance ( $\text{W}/\text{m}^2$ )	1000
	Control mode	PQcontrol
	Reactive power setpoint (kVAr)	0
	Real power setpoint (kW)	30
IC/ $D_4, C_3$	Droop gain	3000
	DC side capacitor (mF)	5
	Filter inductor (mH)	15
	Capacitor ( $\mu\text{F}$ )	1
	Min allowed frequency (Hz)	50
	Max allowed frequency (Hz)	70
	Min DC voltage (V)	590
	Max DC voltage (V)	610
	Current regulator	10+ 62/S

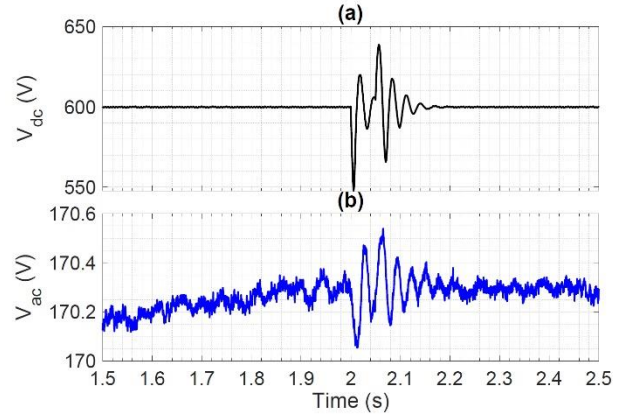
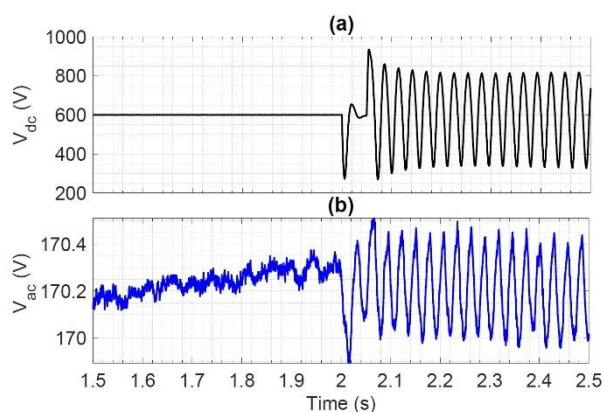


Fig. 2: The voltage magnitude vs. time in scenario I. (a): voltage at node  $D_6$  (b): voltage at node  $C_4$

Table 2: PARAMETERS OF DIFFERENT SIMULATION SCENARIOS

Scenario	Islanded Subgrid	Faulty Node	$R_f(\Omega)$	$T_f$ (ms)
I	DC	$D_5$	10	50
II	DC	$D_5$	1	50
III	AC	$C_2$	0	50
IV	AC	$C_2$	0	100
V	DC & AC	$C_1$	0	100
VI	DC & AC	$D_6$	1	87
VII	DC & AC	$C_{10}$	0	70

In scenario I, the DC subgrid becomes isolated from the MV grid while the AC subgrid remains in the grid-connected mode. The fault inception time is  $t = 2$  s and the fault clearance time is  $T_f = 50$  ms. Fig. 2 demonstrates the voltage magnitudes in scenario I. Scenario II is similar to scenario I where the fault resistance is reduced to  $R_f = 1 \Omega$ , and the corresponding voltage magnitudes are shown in Fig. 3. The results reveal the impact of fault resistance on the transient response of the subgrids. The high resistance fault results in damped oscillations such that the DC voltage returns to the normal range at  $t = 2.15$  s, as shown in Fig. 2. The low resistance fault leads to large-scale oscillations in the DC subgrid and small-scale oscillations in the AC subgrid, as shown in Fig. 3. The wavelet-based time-frequency representation of the DC voltage in scenario II is shown in Fig. 4. This scalogram reveals that the voltage oscillations in the DC subgrid are not damped and consist of a sub-synchronous component at 35 Hz and a super-synchronous component at 70 Hz. The magnitude of the sub-synchronous component is much larger than the magnitude of the super-synchronous component.



**Fig. 3: The voltage magnitude vs. time in scenario II. (a): voltage at node  $D_6$  (b): voltage at node  $C_4$**

A useful case study is obtained where the IC is disconnected from the islanded DC subgrid shortly after the fault clearance. In this case, the voltage magnitudes are shown in Fig. 5. The results indicate the impact of the IC on the post-fault voltages. In this case, the IC operates in the current-controlled mode and injects a certain amount of real power into the DC subgrid to regulate the DC voltage. On the other hand, the ESS uses a voltage regulator (PI controller) and a battery to regulate the voltage at its connection point, i.e.,  $D_5$ . In the presence of the IC, the fault-induced disturbances lead to undamped oscillations as shown in Fig. 3. Such oscillations stem from the circulation of real power due to interactions between the DERs and the IC. Disconnection of the IC eliminates the controller interactions which in turn diminishes the oscillations in almost 40 ms.

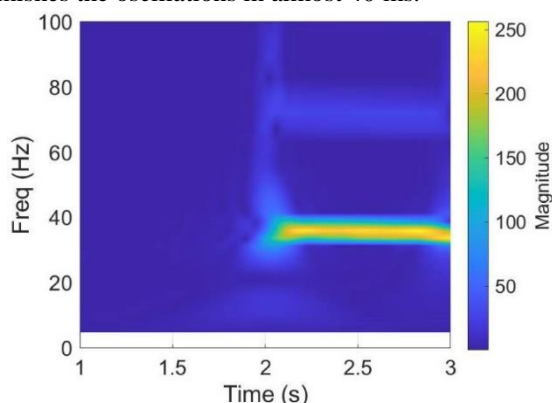


**Fig. 4: Scalogram of the voltage at  $D_6$  in scenario II.**

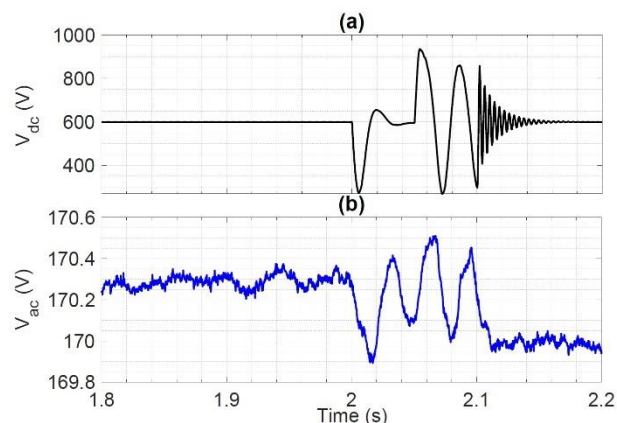


**Fig. 5: The voltage magnitudes in scenario II with the IC disconnected from the DC subgrid at  $t = 2:1$  s (a): voltage at node  $D_6$  (b): voltage at node  $C_4$**

In scenario III, the AC subgrid is disconnected from the MV grid, while the DC subgrid remains connected to the MV grid. Fig. 6 demonstrates the voltage magnitudes in scenario III. Scenario IV is similar to scenario III where the fault clearance time is increased to 100 ms. The voltage magnitudes in scenario IV are shown in Fig. 7. These results reveal the impact of the fault clearance time on the post-fault response of the islanded AC subgrid. In Fig. 6 (b), the fault is cleared after 50 ms and the voltage of the AC subgrid returns to its nominal value at  $t = 2.4$  s, i.e., 350 ms after the instant of fault clearance. However, when the fault clearance time is 100 ms, the voltage of the AC subgrid does not return in the normal range and declines to 0.35 p.u. at  $t = 4$  s, as shown in Fig. 7 (b). This implies that the late isolation or clearance of the faulty node  $C_2$  jeopardizes the voltage stability due to lower inertia of the AC subgrid in the islanded mode of operation.

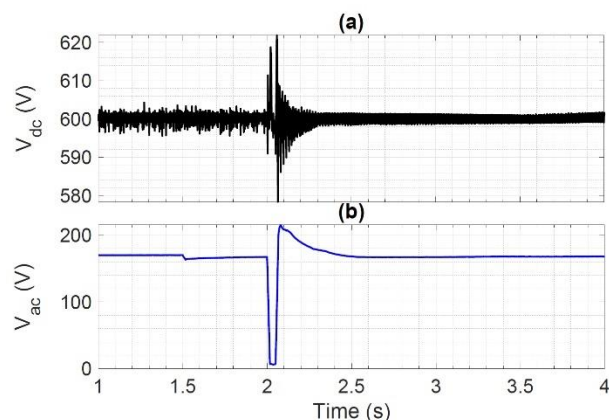


**Fig. 6: The voltage magnitude vs. time in scenario III. (a): voltage at node  $D_6$  (b): voltage at node  $C_4$**

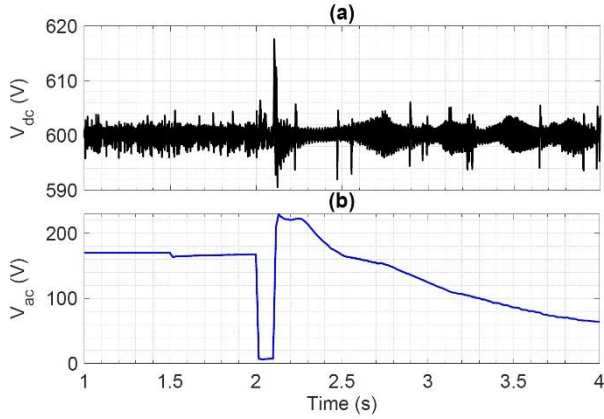


**Fig. 7: The voltage magnitude vs. time in scenario IV. (a): voltage at node  $D_6$  (b): voltage at node  $C_4$**

Moreover, comparison of Fig. 6 (a) with Fig. 7 (a) reveals that a longer fault clearance time in the islanded AC subgrid leads to larger voltage deviations in the grid-connected DC subgrid. For instance, the case of  $T_f = 50$  ms results in DC voltage variations in the range [597,603] V, whereas the case of  $T_f = 100$  ms corresponds to DC voltage variations within the range [594,604] V. It is observed that the maximum (minimum) of post-fault DC voltage in case of  $T_f = 50$  ms is larger (smaller) than the maximum (minimum) of the post-fault DC voltage in case of  $T_f = 100$  ms.

In scenario V, the DC and AC subgrids become isolated from the MV grid. A zero-resistance fault occurs at the node  $C_1$  at the time  $t = 2$  s. Fig. 8 shows the magnitudes of the voltages in scenario V. The results indicate that the voltages of both subgrids are subject to major disturbances after the fault inception time. The AC subgrid incurs severe under-voltage such that the voltage does not return to the normal range after the fault clearance. The DC subgrid, undergoes remarkable voltage fluctuations after the fault clearance, however, the voltage is stabilized and returns to the acceptable range. The ESS in the DC subgrid facilitates the voltage stabilization in the islanded DC subgrid.

The dispersion parameters can be calculated based on other types of time-frequency transforms. For comparison, the S transform [30] is applied on the DC voltage under scenario V, and the resulting DC dispersion is shown in Fig. 9 (b). In this test, the DC dispersion parameter based on the discrete S transform is obtained using the following equation:

$$\delta_{dc,s}(k) = \frac{1}{M-1} \sum_{j=1}^{M-1} |S_{dc}(k,j)|^2 \quad (8)$$

where  $S_{dc}(k,j)$  denotes the S transform coefficient of the discretized signal  $V_{dc}$  and  $M$  is the number of the frequency bins. The discrete time index is related to the wavelet time variable as  $\tau = k/F_s$  where  $F_s$  is the sampling rate of the EMT simulation data. It is seen that the DC dispersion parameters show similar behavior, i.e., they gradually approach zero after the fault clearance, which indicates the DC voltage is recovered successfully. It is concluded that time-frequency analysis methods are promising tools for verification of the impact of faults and the estimation of the CCT in hybrid AC/DC microgrids.

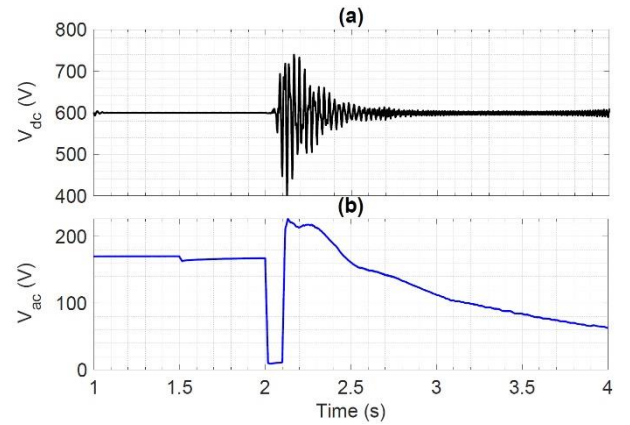


**Fig. 8: The voltage magnitudes vs. time in scenario V. (a): voltage at node  $D_6$  (b): voltage at node  $C_4$**

In scenario VI, the DC and AC subgrids are islanded. The post-fault transient response of the DC subgrid is demonstrated in Fig. 10. It is seen that the fault clearance brings about voltage oscillations that gradually diminish such that the DC voltage is stabilized at around  $t = 2.5$  s. Fig. 10 (b) points out that the DC dispersion can properly quantify the intensity of the constituent components that comprise the post-fault transient response. This result confirms that the low value of the DC dispersion is a qualified indicator of the DC voltage stability and can be used in computation of the CCT.

In scenario VII, the DC and AC subgrids become islanded and the fault is cleared after  $T_f = 70$  ms. The post-fault transient response of the AC subgrid is depicted in Fig. 11. The AC dispersion shown in Fig. 11 (b) reveals the extent of the post-fault perturbations as its value rises from 0 to 0.5 in almost 1 second. The increasing value of the AC dispersion implies that the voltage of the AC subgrid does not return to its nominal value due to the late isolation of the fault in the AC subgrid.

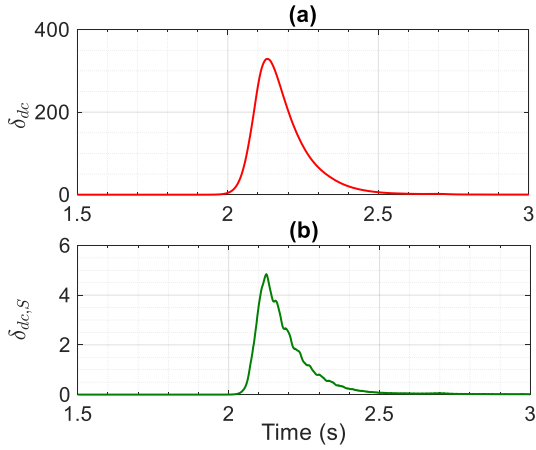


**Fig. 9: Calculation of the DC dispersion parameter in scenario V based on (a): Wavelet Transform and Eq. (5), (b) Discrete S Transform**

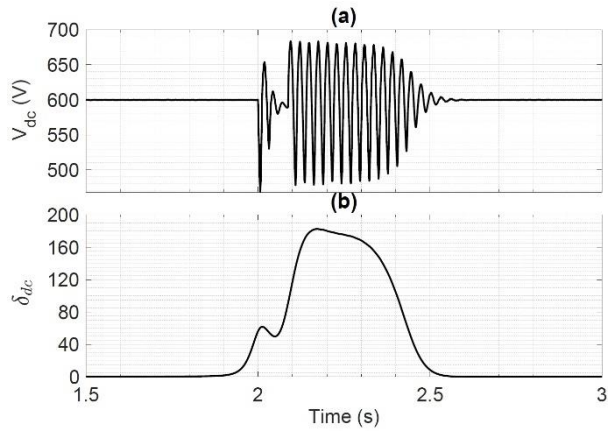


**Fig. 10: The post-fault transient response of the DC subgrid in scenario VI. (a): voltage at node  $D_6$  (b): DC dispersion**

Figs. 12 (a) and (b) respectively demonstrate the estimated CCT for different faulty nodes where the AC and DC subgrids operate in the islanded mode. These results are obtained using the decay time  $\alpha = 1$  s, and the dispersion thresholds  $\Delta_{AC} = 0.1$  and  $\Delta_{DC} = 1$ . The maximum duration for the CCT estimation is  $T_m = 100$  ms and  $T_m = 200$  ms for the DC and AC subgrid, respectively. The search tolerance for both subgrids is  $\beta = 1$  ms. According to (7), the number of simulations required for the CCT estimation are 8 and 9 for the DC and AC subgrid, respectively. In this test, the fault resistance in the AC subgrid is  $0 \Omega$  and the results shown in 12 (a) indicate that node  $C_7$  is the most sensitive node in the islanded AC subgrid as it has the lowest estimated CCT (33 ms). It should be emphasized that the minimum CCT is highly important for the protection scheme of the microgrid and in particular for the IC connection. Backup

and supervisory protection systems can compare the fault isolation time with the estimated CCT to take remedial actions if required.

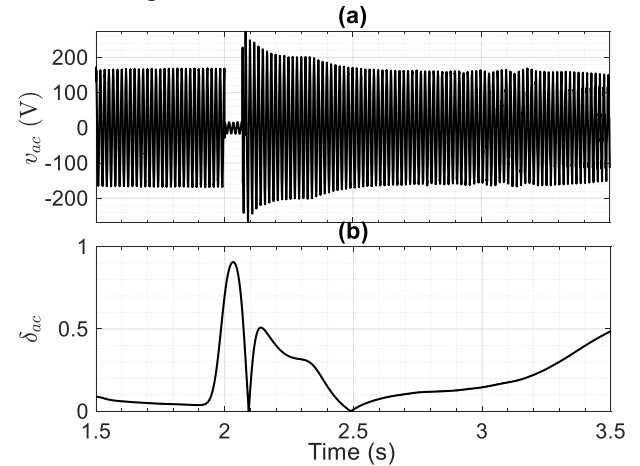


**Fig. 11: The post-fault transient response of the AC subgrid in scenario VII. (a): voltage at node  $C_4$  (b): AC dispersion**

The CCT in the AC subgrid shows large variations, for example, the CCT for node  $C_{11}$  is 120 ms which is much higher than the CCT for node  $C_7$ . The fault resistance in the DC subgrid is  $5 \Omega$  and the results shown in 12 (b) indicate that the CCT in the DC subgrid exhibits small variations with the lowest CCT equal to 86 ms. The results presented in Fig. 12 point out that the CCT can vary significantly depending on the fault location within the islanded subgrid.

## 5. Conclusions

A wavelet-based mechanism is proposed for assessment of the impact of fault duration, resistance and location on the post-fault voltage recovery in hybrid AC/DC microgrids. It is shown that the interactions between the DERs and the ICs may lead to persistent post-fault disturbances in the AC/DC subgrids. It is also observed that if the fault duration exceeds a critical value, then the voltage of the islanded subgrid cannot be recovered. Moreover, time-frequency transforms are employed to derive the AC and DC dispersion parameters for numerical assessments of post-fault voltage recovery. It is indicated that, the nodes connected with a grid-forming system are highly sensitive to the fault-induced disturbances as they exhibit small critical clearance time. Numerical results also point out that, under low-resistance faults, the critical clearance time may vary significantly depending on the fault location in the islanded AC subgrid.

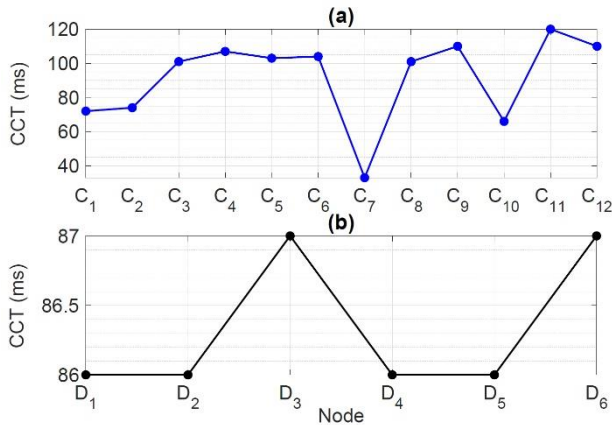


**Fig. 12: CCT for different faulty nodes (a): AC subgrid (b): DC subgrid**

## REFERENCES

- [1] L. E. Zubieta, "Are microgrids the future of energy?: DC microgrids from concept to demonstration to deployment," *IEEE Electrification Magazine*, vol. 4, no. 2, pp. 37-44, Jun. 2016.
- [2] S. K. Sahoo, A. K. Sinha, and N. K. Kishore, "Control techniques in AC, DC, and hybrid AC-DC microgrid: A review," *IEEE J. Emerging Selected Topics Power Electron.*, vol. 6, no. 2, pp. 738-759, Jun. 2018.
- [3] F. Nejabatkhah, Y. W. Li, and H. Tian, "Power quality control of smart hybrid AC/DC microgrids: An overview," *IEEE Access*, vol. 7, pp. 52295-52318, Apr. 2019.
- [4] X. Shen, D. Tan, Z. Shuai, and A. Luo, "Control techniques for bidirectional interlinking converters in hybrid microgrids: Leveraging the advantages of both ac and dc," *IEEE Power Electron. Mag.*, vol. 6, no. 3, pp. 39-47, Sep. 2019.
- [5] S. M. Malik, X. Ai, Y. Sun, C. Zhengqi, and Z. Shupeng, "Voltage and frequency control strategies of hybrid AC/DC microgrid: A review," *IET Generation, Transmission Distribution*, vol. 11, no. 2, pp. 303-313, Jan. 2017.
- [6] A. Gupta, S. Doolla, and K. Chatterjee, "Hybrid AC-DC microgrid: systematic evaluation of control strategies," *IEEE Trans. Smart Grid*, vol. 9, no. 4, pp. 3830-3843, Jul. 2018.
- [7] S. Mirsaedi, X. Dong, S. Shi, and D. Tzelepis, "Challenges, advances and future directions in protection of hybrid AC/DC microgrids," *IET Renewable Power Generation*, vol. 11, no. 12, pp. 1495-1502, Nov. 2017.
- [8] M. Ahmed, L. Meegahapola, A. Vahidnia, and M. Datta, "Analysis and mitigation of low-frequency oscillations in hybrid AC/DC microgrids with dynamic loads," *IET Generation, Transmission Distribution*, vol. 13, no. 9, pp. 1477-1488, Jun. 2019.
- [9] P. V. Dahiwal, and N. M. Pindoriya, "Review on fault management in hybrid microgrid," in *Proc. IEEE Region 10 Symposium (TENSymp)*, Jun. 2019.
- [10] R. Mohanty, and A. K. Pradhan, "Protection of DC and hybrid AC-DC microgrids with ring configuration," in *Proc. International Conference on Power Systems (ICPS)*, Dec. 2017.
- [11] Z. Yongqiang, L. Kang, Z. Quan, H. Minxiao, C. Kai, and J. Yongyong, "Asymmetric fault propagation mechanism on AC side of hybrid microgrid and suppression methods," in *Proc. IEEE Innovative Smart Grid Technologies - Asia (ISGT Asia)*, May 2019.
- [12] Y. Wang, A. Raza, F. P. Mohammed, J. Ravishankar, and T. Phung, "Detection and classification of disturbances in the islanded micro-grid by using wavelet transformation and feature extraction algorithm," *The Journal of Engineering*, vol. 2019, no. 18, pp. 5284-5286, Aug. 2019.
- [13] T. S. Abdelgayed, W. G. Morsi, and T. S. Sidhu, "A new approach for fault classification in microgrids using optimal wavelet functions matching pursuit," *IEEE Trans. Smart Grid*, vol. 9, no. 5, pp. 4838-4846, Sep. 2018.
- [14] J. J. Q. Yu, Y. Hou, A. Y. S. Lam, and V. O. K. Li, "Intelligent fault detection scheme for microgrids with wavelet-based deep neural networks," *IEEE Trans. Smart Grid*, vol. 10, no. 2, pp. 1694-1703, Mar. 2019.
- [15] D. K. J. S. Jayamaha, N. W. A. Lidula, and A. D. Rajapakse, "Wavelet-multi resolution analysis based ANN architecture for fault detection and localization in DC microgrids," *IEEE Access*, vol. 7, pp. 145371-145384, Oct. 2019.
- [16] C. Cepeda, C. Orozco-Henao, W. Percybrooks, J. D. Pulgarin-Rivera, O. D. Montoya, W. Gil-Gonzalez, and J. C. Velez, "Intelligent Fault Detection System for Microgrids," *Energies*, vol. 13, no. 5, Mar. 2020.
- [17] J. Marin-Quintero, C. Orozco-Henao, W. S. Percybrooks, Juan C. Velez, O. D. Montoya, W. Gil-Gonzalez, "Toward an adaptive protection scheme in active distribution networks: Intelligent approach fault detector," *Applied Soft Computing*, vol. 98, Jan. 2021.
- [18] A. Navarro-Rodriguez, P. Garcia, R. Georgious, and J. Garcia, "Adaptive Active Power Sharing Techniques for DC and AC Voltage Control in a Hybrid DC/AC Microgrid," *IEEE Trans. on Industry Applications*, vol. 55, no. 2, pp. 1106-1116, March-April 2019.
- [19] X. Li, Z. Li, L. Guo, J. Zhu, Y. Wang, and C. Wang, "Enhanced Dynamic Stability Control for Low-Inertia Hybrid AC/DC Microgrid With Distributed Energy Storage Systems," *IEEE Access*, vol. 7, pp. 91234-91242, Jul. 2019.
- [20] P. C. Loh, D. Li, Y. K. Chai, and F. Blaabjerg, "Autonomous operation of hybrid microgrid with AC and DC subgrids," *IEEE Trans. Power Electron.*, vol. 28, no. 5, pp. 2214-2223, May 2013.
- [21] S. Peyghami, H. Mokhtari, and F. Blaabjerg, "Autonomous operation of a hybrid AC/DC microgrid with multiple interlinking converters," *IEEE Trans. Smart Grid*, vol. 9, no. 6, pp. 6480-6488, Nov. 2018.
- [22] N. Bottrell, and T. C. Green, "Investigation into the post-fault recovery time of a droop controlled inverter-interfaced microgrid," in *Proc. IEEE 6th International Symposium on Power Electronics for Distributed Generation Systems (PEDG)*, Jun. 2015.
- [23] I. Daubechies, *Ten Lectures on Wavelets*, SIAM: Society for Industrial and Applied Mathematics, 1992.
- [24] J. M. Lilly, and S. C. Olhede, "Higher-Order Properties of Analytic Wavelets," *IEEE Trans. Signal Process.*, vol. 57, no. 1, pp. 146-160, Jan. 2009.

- 
- [25] J. Mahseredjian, S. Denetière, L. Dubé, B. Khodabakhchian and L. Gérin-Lajoie, “On a new approach for the simulation of transients in power systems”, *Electric Power Systems Research*, vol. 77, no. 11, pp. 1514-1520, Sep. 2007.
- [26] J. M. Lilly, and S. C. Olhede. “Generalized Morse wavelets as a superfamily of analytic wavelets.” *IEEE Transactions on Signal Processing* Vol. 60, No. 11, 2012, pp. 6036-6041.
- [27] M. Ganjian-Aboukheili, M. Shahabi, Q. Shafiee, and J. M. Guerrero, “Seamless Transition of Microgrids Operation From Grid-Connected to Islanded Mode”, *IEEE Trans. Smart Grid*, vol. 11, no. 3, pp. 2106-2114, May 2020.
- [28] B. Alghamdi, and C. A. Canizares, “Frequency Regulation in Isolated Microgrids Through Optimal Droop Gain and Voltage Control”, *IEEE Trans. Smart Grid*, Early Access, DOI: 10.1109/TSG.2020.3028472
- [29] Benchmark systems for network integration of renewable and distributed energy resources, CIGRE Task Force C6.04.02, Apr. 2014.
- [30] R. G. Stockwell, L. Mansinha, and R. P. Lowe, “Localization of the complex spectrum: the S transform”, *IEEE Trans. Signal Processing*, vol. 44, no. 4, pp. 998-1001, Apr. 1996.